in Ad-ΔbΔe–infected $^{-/-}$ mice; $P < 0.01$; $n = 6$; Fig. 3 D). Furthermore, the Ad-ΔbΔe infection reduced the incidence of rupture frequency in *periostin*$^{-/-}$ mice (35.0%) compared with that for the Ad-nls-LacZ–treated −/− mice (65.0%; Fig. 3 C). These results demonstrate that periostin ΔbΔe was essential for in vivo recruitment of αSMA-positive fibroblasts to block rupture after AMI. As cell motility and morphology of fibroblasts are associated with the expression of the phosphorylated forms of Akt and focal adhesion kinase (FAK) (26, 27), we examined the phosphorylation of these proteins in the infarct border 5 d after AMI. The amount of phosphorylated Akt was reduced, and only a small amount of phosphorylated FAK was detected in the border of the *periostin*$^{-/-}$ infarcted mice (Fig. 4, A and B, and Fig. S5).

To further investigate the role of periostin in FAK activation and cell motility, we performed immunofluorescence staining for phosphorylated-FAK and rhodamine-phalloidin staining for the actin cytoskeleton in an embryonic mesenchymal cell line, C3H10T1/2, treated or not with periostin ΔbΔe. The presence of periostin ΔbΔe changed the cytoskeletal arrangement and motility of the cells, resulting in dynamic protrusion of their processes (Fig. 4 C). In a time-course

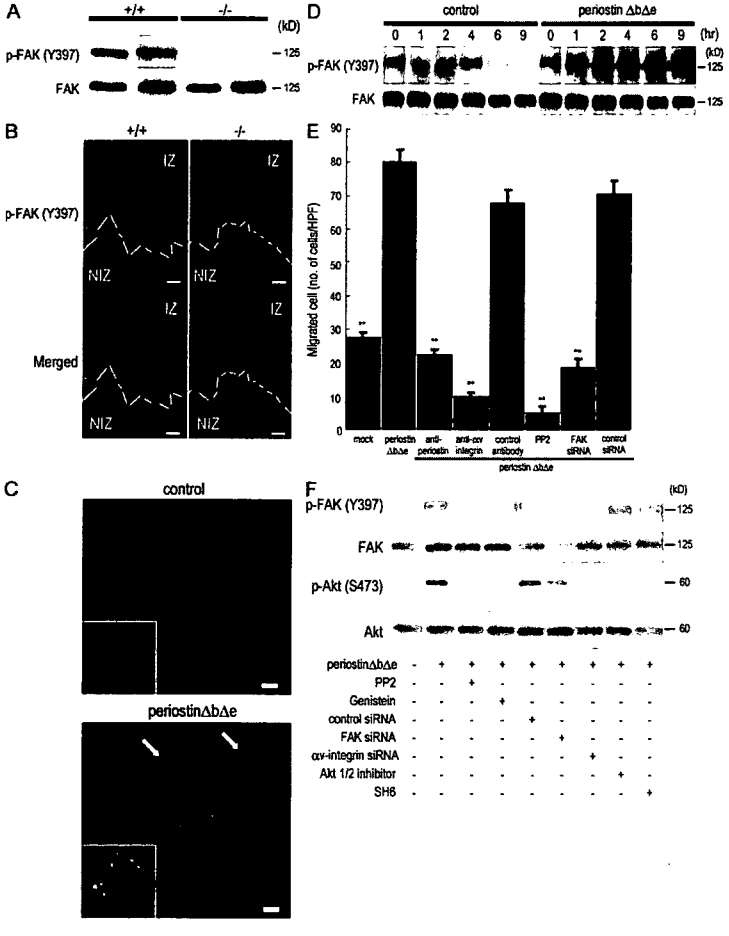

Figure 4. Periostin promotes cell migration through integrin-mediated FAK signaling. (A) Phosphorylation of FAK in infarct LV from *periostin*$^{+/+}$ mice and $^{-/-}$ mice 5 d after AMI. (B) Immunofluorescence for phosphorylated FAK (p-FAK^{Y397}) in the border of infarct LV from *periostin*$^{+/+}$ mice and $^{-/-}$ mice 5 d after AMI. Merged images show an overlay of p-FAK^{Y397} (green) and propidium iodide–stained nuclei (red). The dotted line shows the infarct border. NIZ, noninfarct zone; IZ, infarct zone. (C and D) Promotion of cell spreading and activation of FAK phosphorylation in vitro. The morphology of starved C3H10T1/2 cells was analyzed by immunofluorescence 12 h after adding periostin ΔbΔe (C), and the p-FAK^{Y397} was examined by Western blot analysis at various times after adding periostin ΔbΔe (D). In C, the merged images show an overlay of p-FAK^{Y397} (green) and rhodamine-phalloidin (red), and the arrows point to FAK phosphorylation sites. The insets show higher magnification of the cell processes. (E) Chemotaxis of primary cardiac fibroblasts from *periostin*$^{-/-}$ mice in the absence (mock) or presence of periostin ΔbΔe, detected by an in vitro cell migration assay. Cardiac fibroblasts were significantly activated by periostin ΔbΔe, and treatment with neutralizing antibodies against periostin and αv-integrin, PP2, or FAK siRNAs reduced the cell migration. **, $P < 0.001$ vs. periostin ΔbΔe. Error bars represent the mean ± the SEM. (F) Periostin can stimulate FAK and Akt phosphorylation through integrin signaling. Starved C3H10T1/2 cells were incubated for 1 h with periostin ΔbΔe with or without each siRNA or the FAK and Akt inhibitors. Bars: (B) 100 μm; (C) 20 μm.

experiment, periostin ΔbΔe continuously activated the phosphorylation of FAK for 9 h after the addition of it to serum-starved cell cultures, whereas in the control, the signal had decreased by 6 h (Fig. 4 D). These results demonstrate that periostin ΔbΔe activated FAK phosphorylation and promoted formation of dynamic protrusions. Next, we tested the motility of primary cardiac fibroblasts from *periostin*$^{-/-}$ mice in the presence of periostin ΔbΔe. The result showed that periostin ΔbΔe strongly activated the cell migration of these fibroblasts (Fig. 4 E). Moreover, this migration caused by periostin ΔbΔe was significantly reduced by antibodies against either periostin or αv-integrin; by PP2, which is known as a compound that specifically inhibits adhesion-induced FAK phosphorylation (28); and by knockdown of FAK by siRNA (Fig. 4 E), suggesting that periostin ΔbΔe would activate the cell motility of their fibroblasts by FAK signaling through αv-integrin in mice subjected to AMI. Finally, we inhibited the integrin-mediated FAK pathway by using chemical compounds and siRNAs (Fig. 4 F). FAK inhibitors or siRNA down-regulated the Akt phosphorylation, and Akt inhibitors did not change FAK phosphorylation after stimulation by periostin ΔbΔe, indicating that Akt is a downstream molecule of FAK and periostin ΔbΔe. Moreover, αv-integrin siRNA treatment blocked both FAK and Akt phosphorylation after stimulation by periostin ΔbΔe. These results indicate that periostin ΔbΔe can stimulate FAK and Akt phosphorylation through αv-integrin.

We demonstrated that in the case of periostin deficiency, the collagen amount was reduced in the infarct myocardium, resulting in frequent cardiac rupture in the AMI. Our results, together with the previous findings by Norris et al. (7) on the role of periostin in collagen fibrillogenesis of skin and tendon, strongly suggest that fibrillar collagen formation, which contributes essentially to a mechanically stable scar formation, was impaired in the early stage of MI in the periostin deficiency, resulting in a high rate of cardiac rupture. Furthermore, we have found that the reduced mechanical strength, rupture of the infarct region, and repression of LV dilation in periostin deficiency were most likely caused by a reduced number of cardiac fibroblasts and by the insufficient creation of a durable collagen network caused by a lower rate of collagen synthesis and cross-linking. To reveal more about the importance of collagen production or collagen cross-linking for protection against heart rupture, after AMI, we treated mice with an inhibitor of lysyl oxidase, thus inhibiting collagen cross-linking. Interestingly, the data showed a high amount of collagen production with a larger number of vimentin-positive cells in the infarct region, resulting in effective blockage of heart rupture (unpublished data). These data suggest that periostin-stimulated migration of cardiac fibroblasts into the infarct region, the cells of which produce a high amount of collagen, is more essential than collagen cross-linking by periostin.

The expression of TGFβ was markedly up-regulated in the infarct border during the scar formation phase after AMI, and the phosphorylation of smad 2/3 was consequently increased (unpublished data), whereas there was no significant difference in the TGFβ transcription level between *periostin*$^{+/+}$ and $^{-/-}$ mice; TGFβ also enhanced the periostin expression in the infarct border after AMI because anti-TGFβ antibody treatment blocked the periostin expression (Fig. S6, available at http://www.jem.org/cgi/content/full/jem.20071297/DC1). The expression of both TGFβ and periostin is up-regulated by angiotensin II and attenuated by angiotensin receptor blockers after AMI (29, 30), suggesting that periostin may play a role via angiotensin II-TGFβ signaling. The combined results on the biomechanical properties and the collagen content of the isolated infarct heart support the concept that the periostin-linked collagen fibrous skeleton is an important determinant of cardiac rupture.

The results given here indicate that periostin signals activate cell migration of cardiac fibroblasts from outside into the infarct region through FAK phosphorylation, and then the migrated cells differentiate into αSMA-positive fibroblasts, resulting in strengthening of the stiffness of the LV wall through collagen synthesis after AMI. FAK is known to be involved in tyrosine phosphorylation during integrin-mediated signaling, and this molecule plays an important role in the response of migrating cells to mechanical stress (31). Recently, FAK has been implicated as a downstream target associated with angiotensin II–stimulated cell migration (32). The mechanism underlying the periostin action of promoting the recruitment of cardiac fibroblasts followed by healing of the infarct region appears to involve activation of the FAK pathway, indicating that the periostin-induced increase in FAK phosphorylation in the infarct myocardium enhanced the motility of these fibroblasts. In contrast, three-dimensional culture studies imply that the matrix stiffness regulates cell fate by modulating integrin signaling (31, 33). Considering these accumulated results, we suggest that periostin is mainly produced by fibroblasts through angiotensin II–TGFβ signaling and may convey pathologically rapid reinforced mechanical signals to FAK-integrin signaling after AMI. The fibroblastic cells activated by these signals secrete periostin, which in turn increases their motility, contractility, and synthesis of ECM proteins, thus promoting further recruitment and activation of fibroblasts. Periostin may serve as the trigger of these feedback mechanisms in the ongoing healing processes. Additional studies to elucidate in more detail the characteristics of cardiac fibroblasts may lead to a deeper understanding of the role of periostin after AMI, as well as aid in identifying the molecular targets of therapies to augment cardiac performance and wall stiffness after AMI.

MATERIALS AND METHODS

Preparation of rabbit polyclonal antibodies against periostin. We raised polyclonal RD1 antibodies against periostin by using the peptide DNLDSDIRRGLESNVN (representing aa 143–158 of human periostin) for human periostin and the peptide ENLDSDIRRGLENNVN (representing aa 145–160 of mouse periostin) for mouse periostin. The antibodies were affinity-purified by using the respective immunogenic peptide.

Histology, immunostaining, and electron microscopy. Human tissue samples were obtained during autopsy and fixed in 4% neutral formalin or 20% formalin. A total of 41 cases, ranging from a fetus to an 89-yr-old patient, including 15 cases of myocardial infarction, were examined. All the cases were approved for use in research by the Ethics Committee of the

University of Tokyo. After having been embedded in paraffin, specimens were cut at a 4-μm thickness. Hematoxylin and eosin, elastica von Gieson, and Azan staining procedures were performed. Immunohistochemistry by the ABC method was done by using an i6000 apparatus (Biogenex).

For histological analysis of the infarcted mice, the animals were killed at 1, 2, 3, 4, 5, 7, 14, or 28 d after surgery under anesthesia, and were perfusion fixed with 4% paraformaldehyde at physiological pressure. Fixed hearts were sectioned transversely into three equal segments from their apex to base and cryoembedded or embedded in paraffin. 4-μm-thick sections were used for histological analysis or for immunostaining. Antibodies against αv-integrin (Laboratory Vision), αSMA (Sigma-Aldrich), FAK (BD Biosciences), pY397FAK (Invitrogen), pS473Akt (Cell Signaling Technology), Akt (Cell Signaling Technology), collagen I (Novotec), fibronectin (34), Ki67 (YLEM), active caspase3 (Promega), vimentin (PROGEN), smooth muscle myosin-1 (SM1; Kyowa Hakko Ltd.), and Mac3 (BD Biosciences) were used for immunostaining. Antigen unmasking techniques were not performed, except for anti–αv-integrin. For immunostaining of pY397FAK and pS473Akt, the Catalyzed Signal Amplification system was used (Dako). In the case of fluorescence studies, the signals were observed under a confocal microscope (FLUOVIEW FV1000; Olympus).

Sections of infarcted heart were generated from 6 *periostin*$^{+/+}$ and 6 $^{-/-}$ male mice at 5 and 28 d after AMI, and they were prepared for electron microscopy as previously described (35). Sham-operated mice were used for the control. Collagen fibril diameters were measured in scanned images generated from electron micrographs with Image J software. Collagen fibrils and the number of vimentin-positive or αSMA-positive cells in at least 6 fields derived from each of the basement-, mid-, and apex-part of the infarct region of heart sections were quantified (6 mice per group). Animal studies were conducted under a protocol approved by the Institutional Animal Use and Care Committee.

Quantification of collagen cross-links and collagen contents. Snap-frozen infarct tissues from *periostin*$^{+/+}$ and $^{-/-}$ mice were used. Pyridinoline and hydroxyproline contents were determined by the previously described HPLC method (36).

Adenovirus-mediated gene transfer. Construction of Ad-nlsLacZ and Ad-periostin ΔbΔe vectors was performed by use of an Adeno-X Expression System 2 (BD Biosciences). The virus purification method used, involving cesium chloride ultracentrifugation, was previously described (37). 1 d before LAD ligation, a volume of 100 μl containing 1.6×10^{10} PFU of Ad-nlsLacZ or Ad-periostin ΔbΔe virus was injected into a tail vein of male *periostin*$^{-/-}$ mice.

Statistical analysis. All numerical results were presented as the mean ± the SEM. Statistical analyses of the echocardiography and cell migration assay were performed with a Student's unpaired *t* test. Cardiac rupture frequency was compared by the χ^2 test. Survival curves after AMI were obtained by the Kaplan-Meier method, and compared by the log-rank test. Differences were considered significant at $P < 0.05$.

Online supplemental material. Fig. S1 shows the confirmation of the periostin expression in cardiac fibroblasts. Fig. S2 indicates the generation of *periostin*$^{-/-}$ mice. Fig. S3 shows the immunofluorescence analysis of fibronectin after AMI. Fig. S4 shows immunofluorescence analysis for gene-transferred *periostin*$^{-/-}$ infarct heart. Fig. S5 depicts the analysis for the phosphorylation of Akt after AMI. Fig. S6 shows a cause-and-effect relationship between TGFβ and periostin after AMI. Table S1 provides the echocardiographic data. Full methods and associated references are available in the Supplemental materials and methods. The online version of this article is available at http://www.jem.org/cgi/content/full/jem.20071297/DC1.

The authors thank M. Ikumi and E. Ikeno for technical assistance in generating knockout mice; S. Matsumura and M. Yoshioka for their technical help in the LV rupture threshold study; and S. Sakaguchi for her support, patience, and comprehension.

This research was supported by grants-in-aid from the Ministry of Education, Culture, Sports, Science, and Technology of Japan to A. Kudo and Y. Saga.

The authors have no conflicting financial interests.

Submitted: 25 June 2007
Accepted: 17 December 2007

REFERENCES

1. Horiuchi, K., N. Amizuka, S. Takeshita, H. Takamatsu, M. Katsuura, H. Ozawa, Y. Toyama, L.F. Bonewald, and A. Kudo. 1999. Identification and characterization of a novel protein, periostin, with restricted expression to periosteum and periodontal ligament and increased expression by transforming growth factor beta. *J. Bone Miner. Res.* 14:1239–1249.
2. Gillan, L., D. Matei, D.A. Fishman, C.S. Gerbin, B.Y. Karlan, and D.D. Chang. 2002. Periostin secreted by epithelial ovarian carcinoma is a ligand for alpha(V)beta(3) and alpha(V)beta(5) integrins and promotes cell motility. *Cancer Res.* 62:5358–5364.
3. Bao, S., G. Ouyang, X. Bai, Z. Huang, C. Ma, M. Liu, R. Shao, R.M. Anderson, J.N. Rich, and X.F. Wang. 2004. Periostin potently promotes metastatic growth of colon cancer by augmenting cell survival via the Akt/PKB pathway. *Cancer Cell.* 5:329–339.
4. Lindner, V., Q. Wang, B.A. Conley, R.E. Friesel, and C.P.H. Vary. 2005. Vascular injury induces expression of periostin: implications for vascular cell differentiation and migration. *Arterioscler. Thromb. Vasc. Biol.* 25:77–83.
5. Li, G., S. Oparil, J.M. Sanders, L. Zhang, M. Dai, L.B. Chen, S.J. Conway, C.A. McNamara, and I.J. Sarembock. 2006. Phosphatidylinositol-3-kinase signaling mediates vascular smooth muscle cell expression of periostin in vivo and in vitro. *Atherosclerosis.* 188:292–300.
6. Butcher, J.T., R.A. Norris, S. Hoffman, C.H. Mjaatvedt, and R.R. Markwald. 2007. Periostin promotes atrioventricular mesenchyme matrix invasion and remodeling mediated by integrin signaling through Rho/PI 3-kinase. *Dev. Biol.* 302:256–266.
7. Norris, R.A., B. Damon, V. Mironov, V. Kasyanov, A. Ramamurthi, R. Moreno-Rodriguez, T. Trusk, J.D. Potts, R.L. Goodwin, J. Davis, et al. 2007. Periostin regulates collagen fibrillogenesis and the biomechanical properties of connective tissues. *J. Cell. Biochem.* 101:695–711.
8. Kruzynska-Frejtag, A., M. Machnicki, R. Rogers, R.R. Markwald, and S.J. Conway. 2001. Periostin (an osteoblast-specific factor) is expressed within the embryonic mouse heart during valve formation. *Mech. Dev.* 103:183–188.
9. Stanton, L.W., L.J. Garrard, D. Damm, B.L. Garrick, A. Lam, A.M. Kapoun, Q. Zheng, A.A. Protter, G.F. Schreiner, and R.T. White. 2000. Altered patterns of gene expression in response to myocardial infarction. *Circ. Res.* 86:939–945.
10. Urasawa, K., I. Yoshida, C. Takagi, H. Onozuka, T. Mikami, H. Kawaguchi, and A. Kitabatake. 1996. Enhanced expression of beta-adrenergic receptor kinase 1 in the hearts of cardiomyopathic Syrian hamsters, BIO53.58. *Biochem. Biophys. Res. Commun.* 219:26–30.
11. Wang, D., S. Oparil, J.A. Feng, P. Li, G. Perry, L.B. Chen, M. Dai, S.W. John, and Y.F. Chen. 2003. Effects of pressure overload on extracellular matrix expression in the heart of the atrial natriuretic peptide-null mouse. *Hypertension.* 42:88–95.
12. Katsuragi, N., R. Morishita, N. Nakamura, T. Ochiai, Y. Taniyama, Y. Hasegawa, K. Kawashima, Y. Kaneda, T. Ogihara, and K. Sugimura. 2004. Periostin as a novel factor responsible for ventricular dilation. *Circulation.* 110:1806–1813.
13. Bujak, M., and N.G. Frangogiannis. 2007. The role of TGF-beta signaling in myocardial infarction and cardiac remodeling. *Cardiovasc. Res.* 74:184–195.
14. Sun, Y., and K.T. Weber. 2000. Infarct scar: a dynamic tissue. *Cardiovasc. Res.* 46:250–256.
15. Virag, J.I., and C.E. Murry. 2003. Myofibroblast and endothelial cell proliferation during murine myocardial infarct repair. *Am. J. Pathol.* 163:2433–2440.
16. Tomasek, J.J., G. Gabbiani, B. Hinz, C. Chaponnier, and R.A. Brown. 2002. Myofibroblasts and mechano-regulation of connective tissue remodelling. *Nat. Rev. Mol. Cell Biol.* 3:349–363.
17. Heymans, S., A. Luttun, D. Nuyens, G. Theilmeier, E. Creemers, L. Moons, G.D. Dyspersin, J.P.M. Cleutjens, M. Shipley, A. Angellilo,

et al. 1999. Inhibition of plasminogen activators or matrix metalloproteinases prevents cardiac rupture but impairs therapeutic angiogenesis and causes cardiac failure. *Nat. Med.* 5:1135–1142.
18. Matsumura, S.-I., S. Iwanaga, S. Mochizuki, H. Okamoto, S. Ogawa, and Y. Okada. 2005. Targeted deletion or pharmacological inhibition of MMP-2 prevents cardiac rupture after myocardial infarction in mice. *J. Clin. Invest.* 115:599–609.
19. Matsusaka, H., T. Ide, S. Matsushima, M. Ikeuchi, T. Kubota, K. Sunagawa, S. Kinugawa, and H. Tsutsui. 2006. Targeted deletion of p53 prevents cardiac rupture after myocardial infarction in mice. *Cardiovasc. Res.* 70:457–465.
20. Nahrendorf, M., K. Hu, S. Frantz, F.A. Jaffer, C.-H. Tung, K.-H. Hiller, S. Voll, P. Nordbeck, D. Sosnovik, S. Gattenlohner, et al. 2006. Factor XIII deficiency causes cardiac rupture, impairs wound healing, and aggravates cardiac remodeling in mice with myocardial infarction. *Circulation.* 113:1196–1202.
21. Askari, A.T., M.-L. Brennan, X. Zhou, J. Drinko, A. Morehead, J.D. Thomas, E.J. Topol, S.L. Hazen, and M.S. Penn. 2003. Myeloperoxidase and plasminogen activator inhibitor 1 play a central role in ventricular remodeling after myocardial infarction. *J. Exp. Med.* 197:615–624.
22. Sun, M., F. Dawood, W.-H. Wen, M. Chen, I. Dixon, L.A. Kirshenbaum, and P.P. Liu. 2004. Excessive tumor necrosis factor activation after infarction contributes to susceptibility of myocardial rupture and left ventricular dysfunction. *Circulation.* 110:3221–3228.
23. Ichihara, S., T. Senbonmatsu, E. Price Jr., T. Ichiki, F.A. Gaffney, and T. Inagami. 2002. Targeted deletion of angiotensin II type 2 receptor caused cardiac rupture after acute myocardial infarction. *Circulation.* 106:2244–2249.
24. Michael, L.H., M.L. Entman, C.J. Hartley, K.A. Youker, J. Zhu, S.R. Hall, H.K. Hawkins, K. Berens, and C.M. Ballantyne. 1995. Myocardial ischemia and reperfusion: a murine model. *Am. J. Physiol.* 269:H2147–H2154.
25. Lindsley, A., W. Li, J. Wang, N. Maeda, R. Rogers, and S.J. Conway. 2005. Comparison of the four mouse fasciclin-containing genes expression patterns during valvuloseptal morphogenesis. *Gene Expr. Patterns.* 5:593–600.
26. Stambolic, V., and J.R. Woodgett. 2006. Functional distinctions of protein kinase B/Akt isoforms defined by their influence on cell migration. *Trends Cell Biol.* 16:461–466.
27. Mitra, S.K., D.A. Hanson, and D.D. Schlaepfer. 2005. Focal adhesion kinase: in command and control of cell motility. *Nat. Rev. Mol. Cell Biol.* 6:56–68.
28. Hakuno, D., T. Takahashi, J. Lammerding, and R.T. Lee. 2005. Focal adhesion kinase signaling regulates cardiogenesis of embryonic stem cells. *J. Biol. Chem.* 280:39534–39544.
29. Iekushi, K., Y. Taniyama, J. Azuma, N. Katsuragi, N. Dosaka, F. Sanada, N. Koibuchi, K. Nagao, T. Ogihara, and R. Morishita. 2007. Novel mechanisms of valsartan on the treatment of acute myocardial infarction through inhibition of the antiadhesion molecule periostin. *Hypertension.* 49:1409–1414.
30. Berk, B.C., K. Fujiwara, and S. Lehoux. 2007. ECM remodeling in hypertensive heart disease. *J. Clin. Invest.* 117:568–575.
31. Wang, H.-B., M. Dembo, S.K. Hanks, and Y.-l. Wang. 2001. Focal adhesion kinase is involved in mechanosensing during fibroblast migration. *Proc. Natl. Acad. Sci. USA.* 98:11295–11300.
32. Baudino, T.A., W. Carver, W. Giles, and T.K. Borg. 2006. Cardiac fibroblasts: friend or foe? *Am. J. Physiol. Heart Circ. Physiol.* 291:H1015–H1026.
33. Bershadsky, A.D., N.Q. Balaban, and B. Geiger. 2003. Adhesion-dependent cell mechanosensitivity. *Annu. Rev. Cell Dev. Biol.* 19:677–695.
34. Arai, S., N. Amizuka, Y. Azuma, S. Takeshita, and A. Kudo. 2003. Osteoclastogenesis-related antigen, a novel molecule on mouse stromal cells, regulates osteoclastogenesis. *J. Bone Miner. Res.* 18:686–695.
35. Kii, I., N. Amizuka, L. Minqi, S. Kitajima, Y. Saga, and A. Kudo. 2006. Periostin is an extracellular matrix protein required for eruption of incisors in mice. *Biochem. Biophys. Res. Commun.* 342:766–772.
36. Saito, M., K. Marumo, K. Fujii, and N. Ishioka. 1997. Single-column high-performance liquid chromatographic-fluorescence detection of immature, mature, and senescent cross-links of collagen. *Anal. Biochem.* 253:26–32.
37. Ugai, H., T. Yamasaki, M. Hirose, K. Inabe, Y. Kujime, M. Terashima, B. Liu, H. Tang, M. Zhao, T. Murata, et al. 2005. Purification of infectious adenovirus in two hours by ultracentrifugation and tangential flow filtration. *Biochem. Biophys. Res. Commun.* 331:1053–1060.

The Journal of Toxicological Sciences (J. Toxicol. Sci.)
Vol.33, No.1, 105-116, 2008

Original Article

Induction of mesothelioma in p53+/– mouse by intraperitoneal application of multi-wall carbon nanotube

Atsuya Takagi[1], Akihiko Hirose[2], Tetsuji Nishimura[3], Nobutaka Fukumori[4], Akio Ogata[4], Norio Ohashi[4], Satoshi Kitajima[1] and Jun Kanno[1]

[1]Division of Cellular and Molecular Toxicology, Biological Safety Research Center, National Institute of Health Sciences, 1-18-1 Kamiyoga, Setagaya-ku, Tokyo 158-8501, Japan
[2]Division of Risk Assessment, Biological Safety Research Center, National Institute of Health Sciences, 1-18-1 Kamiyoga, Setagaya-ku, Tokyo 158-8501, Japan
[3]Division of Environmental Chemistry, National Institute of Health Sciences, 1-18-1 Kamiyoga, Setagaya-ku, Tokyo 158-8501, Japan
[4]Department of Environmental Health and Toxicology, Tokyo Metropolitan Institute of Public Health, 3-24-1 Hyakunin-cho, Shinjuku-ku, Tokyo 169-0073, Japan

(Received November 20, 2007; Accepted December 9, 2007)

ABSTRACT — Nanomaterials of carbon origin tend to form various shapes of particles in micrometer dimensions. Among them, multi-wall carbon nanotubes (MWCNT) form fibrous or rod-shaped particles of length around 10 to 20 micrometers with an aspect ratio of more than three. Fibrous particles of this dimension including asbestos and some man-made fibers are reported to be carcinogenic, typically inducing mesothelioma. Here we report that MWCNT induces mesothelioma along with a positive control, crocidolite (blue asbestos), when administered intraperitoneally to p53 heterozygous mice that have been reported to be sensitive to asbestos. Our results point out the possibility that carbon-made fibrous or rod-shaped micrometer particles may share the carcinogenic mechanisms postulated for asbestos. To maintain sound activity of industrialization of nanomaterials, it would be prudent to implement strategies to keep good control of exposure to fibrous or rod-shaped carbon materials both in the workplace and in the future market until the biological/ carcinogenic properties, especially of their long-term biodurability, are fully assessed.

Key words: Multi-wall carbon nanotube (MWCNT); Asbestos; Fullerene; Mesothelioma; P53 heterozygous mouse; Micrometer particles

INTRODUCTION

A rapid increase in the usage of nanomaterials in consumer products and medical applications in the near future underlines the importance of understanding its potential toxicity to people and the environment (Lam *et al.*, 2006; Donaldson *et al.*, 2006). Among them, carbon nanotubes and fullerenes have been one of the most extensively researched and developed nanoparticles. Carbon nanoparticles tend to aggregate into micrometer particles due to their cohesive characteristics (Lam *et al.*, 2006; Luo *et al.* 2004). And they are considered to be very stable in the organism. These two elements lead us toxicologists to consider a concern of the chronic toxicity of micrometer-sized particles before any consideration is made for their pure nanometer-sized properties in our body. Once inside the body, the long-lasting scavenging and inflammatory activities towards the non-degradable micrometer-sized particles would lead to the continuous oxidative stress at their deposit sites, which eventually lead to tissue destruction and, on some occasion, carcinogenesis (Coussens and Werb, 2002). Additional concern is given to the fibrous or

Correspondence: Jun Kanno (E-mail: kanno@nihs.go.jp)

rod-shaped particles of micrometer length that share the dimension of asbestos reported to be carcinogenic to humans and experimental animals (Hei *et al.*, 2006; WHO,1986, 1998). Another factor reported to relate with carcinogenic potency of asbestos is the iron (Fe) content. The most potent asbestos (crocidolite or blue asbestos) contains the highest amount of Fe (WHO, 1986). It is explained that Fenton reaction would accelerate the generation of oxygen radical species that lead to carcinogenesis (Jiang *et al.*, 2006; Gulumian and Wyk, 1987).

MWCNTs form micrometer-sized particles of fiber or rod-shape. The diameter ranges from 0.01 to 0.2 micrometer (Hou *et al.*, 2003) and lengths may reach tens of micrometers that correspond to the size and shape of asbestos. Additionally, some CNTs are reported to contain a considerable amount of Fe due to its manufacturing process (Lam *et al.*, 2006). Deduced from those factors, we hypothesized that MWCNT might have carcinogenic potency similar to asbestos when administered to organisms via the same route of exposure. Here, we adopted a short-term bioassay, i.e., the p53 heterozygous mouse intraperitoneal exposure model reported to be sensitive to asbestos and develop mesotheliomas fast (Marsella *et al.*, 1997; Vaslet *et al.*, 2002). This mouse model has been reported to be sensitive not only to genotoxic carcinogens (Pritchard *et al.*, 2003) but also to reactive oxygen species (ROS)-related carcinogenesis (Tazawa *et al.*, 2007) and therefore fits with the postulated carcinogenesis mechanisms of asbestos and asbestos-like particles (Marsella *et al.*, 1997; Vaslet *et al.*, 2002).

MATERIALS AND METHODS

Experimental animals

The p53-heterozygos (p53(+/–)) mice were generously given by Dr. S. Aizawa (Tsukada *et al.*,1993). This p53 (+/–) mice were bred with normal wild-type C57BL/6 females (SLC, Shizuoka, Japan). After more than 20 generations of backcrossing, seventy-six male p53(+/–) mice of an age of 9 to 11 weeks were used in this experiment (nineteen per group). All mice were housed individually under specific pathogen-free conditions, with a 12 hr light-dark cycle at the animal facility of NIHS. They were given tap water and autoclaved CRF-1 pellets (Oriental Yeast Co., ltd.) *ad libitum*. Experiments were humanely conducted under the regulation and permission of the Animal Care and Use Committee of the National Institute of Health Sciences (NIHS), Tokyo, Japan.

Histology

For evaluation of carcinogenicity, visceral organs including liver, kidney, spleen, lung, digestive tract and macroscopic tumors (*en bloc* in case of severe peritoneal adhesion) were fixed in 10% neutral buffered formalin. After conventional processing, paraffin-embedded sections were stained with hematoxylin and eosin (H&E) and

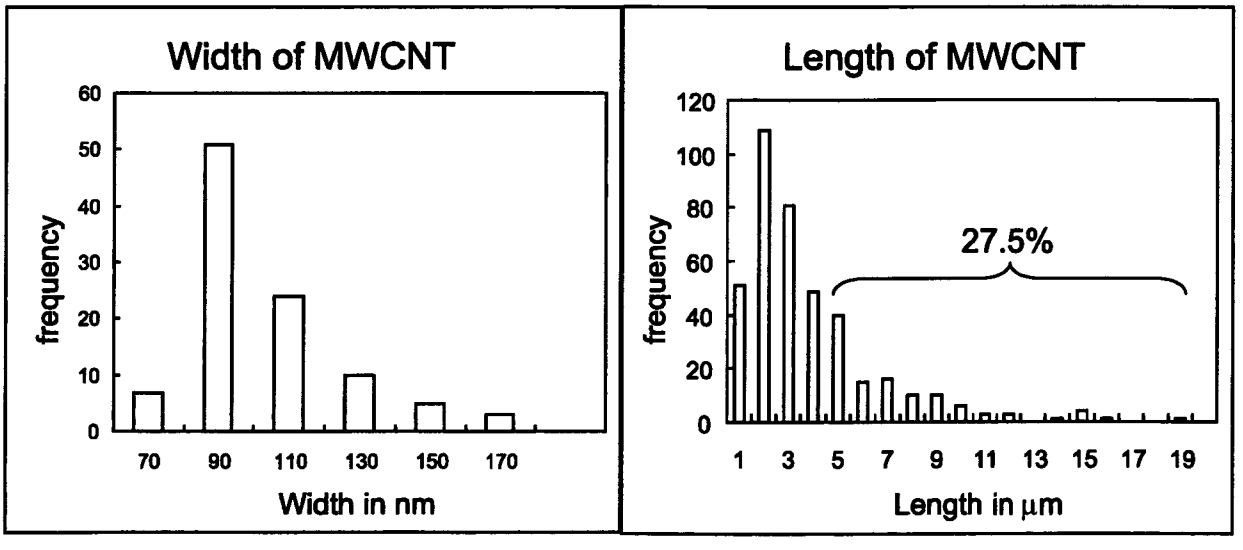

Fig. 1. Width and length distribution of MWCNT:
Width and length distribution of MWCNT (MITSUI MWCNT-7, Lot NO. 060125-01k) was measured at Tokyo Metropolitan Institute of Public Health. The average width was about 100 nm, and 27.5% of the particles were longer than 5 micrometer.

examined histopathologically under a light microscope.

Materials

Multi-wall carbon nanotube (MITSUI MWCNT-7, Lot NO. 060125-01k), UICC-grade Crocidolite (NIHS material stock), and fullerene (C_{60}, Nanom purple, Frontier Carbon Corporation, Tokyo, Japan) were used in this study.

The number of particles per weight and size distribution of MWCNT was determined as follows: 1.03 mg of MWCNT was suspended in 5 ml of 5%Triton X-100 (Qbiogene, CA, USA) and sonicated for 30 min, immediately diluted x100 by 5%TX-100, and then an aliquot of 5 microliters was mounted on a glass plate. The plate was heated up to 480 °C for 20 min by an electric oven, metallized by platinum and palladium, and subjected to scanning electron microscope observation. All visual fields were photographed. Number and length of the particles were measured on the enlarged photo prints. As a result, one gram of MWCNT corresponded to 3.55×10^{11} particles. The length and width distribution is shown in Fig. 1. The number of particles per weight of the UICC Crocidolite was reported as 2.93×10^{12} fibers/g (Moalli *et al.*, 1987). The contents of elements in the MWCNT were determined by collision type inductively coupled plasma mass spectrometer (ICP-MS 7500ce, Agilent Technologies, Inc. Santa Clara, CA, USA) and combustion ion chromatography (DX-120, Dionex Corporation, Sunnyvale, CA, USA). The average content of Fe was about 3,500 ppm (0.35%) by a microwave-assisted dissolution procedure with a mix-

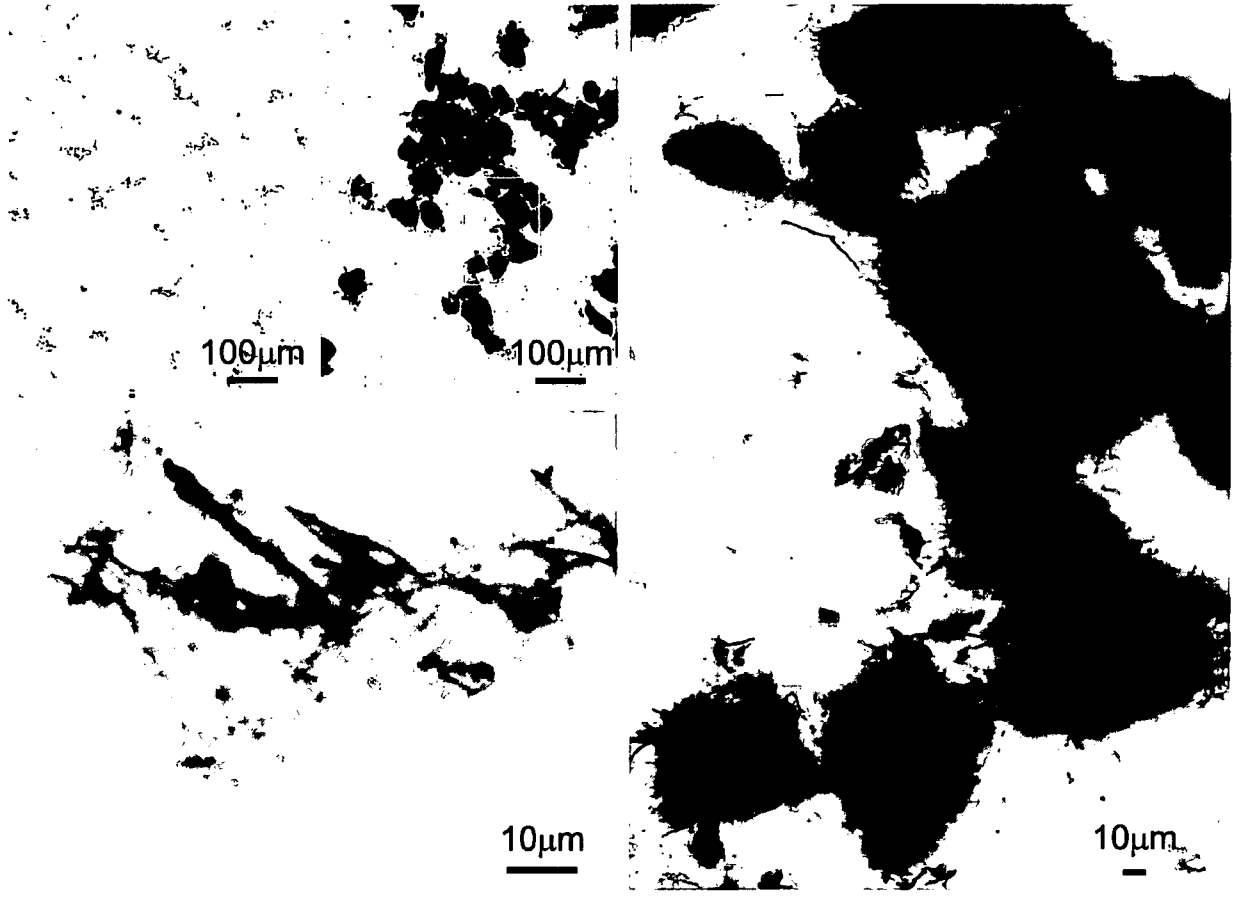

Fig. 2. Light microscopic view of administered MWCNT:
Light microscopic view of sonicated MWCNT sample suspension mounted on slide glasses. a) Well-dispersed area of the preparation. b) Close-up view of the boxed area in a). Fine fiber or rod-shaped particles longer than 10 micrometers are seen. c) Aggregated MWCNT. d) Close-up view of the boxed area in c) Aggregates are 50 to 200 micrometers in dimensions.

ture of nitric acid and perchloric acid. Sulfur content was about 470 ppm. Chlorine was 20 ppm and fluorine and bromine were below detection levels (5 and 40 ppm, respectively).

Preparation of particle suspension

MWCNT, crocidolite and fullerene were suspended at a concentration of 3 mg/ml to 0.5% methyl cellulose (Shin-Etsu Chemical Co., Ltd.) solution and autoclaved (121 °C, 15 min). After addition of Tween 80 (Tokyo Chemical Industry Co., Ltd.; final 1.0% conc.), the solutions were subjected to sonication by ultrasonic homogenizer (VP30s, TAITEC Co. Japan) (cf. Fig. 2).

Treatment of mice

Nineteen male p53 (+/−) mice at the age of 9 to 11 weeks were given single i.p. injection of 1×10^9 of MWCNT particles (corresponding to 3 mg/head) in 1 ml suspension. The number of the particles was set to a moderate value of the reported ranges (Roller *et al.*, 1997) which corresponds to the maximum value recommended by the draft guideline for man-made mineral fibers (Bernstein and Riego Sintes, 1999). Another 19 mice were given single i.p. injection of 3 mg/head suspension (1 ml) of fullerene, and as a positive control of this carcinogenesis study, another 19 mice were given 1×10^{10} of crocidolite in 1 ml of suspension (corresponds to 3 mg/head) at the first day of experiment. Vehicle solution (1 ml) was given to 19 mice as negative controls. Satellite groups consisting

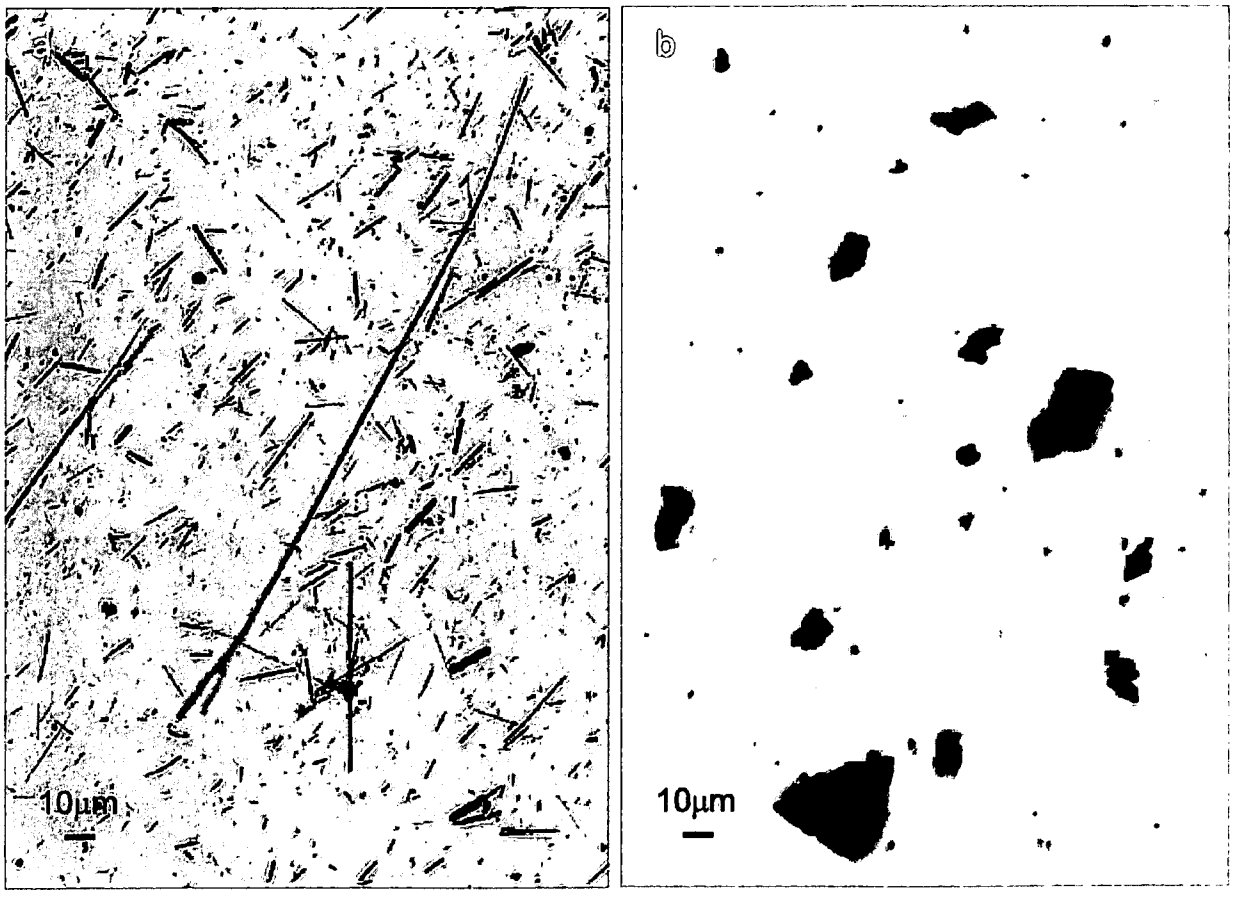

Fig. 3. Light microscopic views of administered crocidolite and fullerene:
Light microscopic views of administered crocidolite and fullerene. a) Crocidolite sample consisting of various lengths of rod-shaped particles. b) Fullerene sample consisted of sand grain-like particles of sizes ranging up to 50 micrometers.

Mesothelioma by MWCNT in p53 +/– mouse.

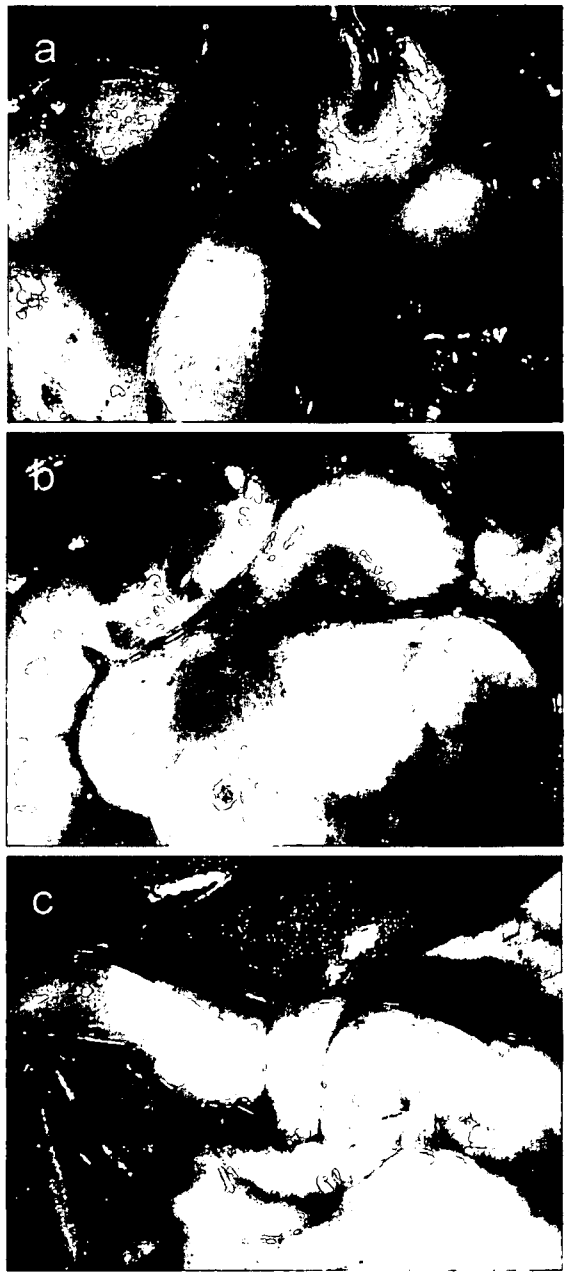

Fig. 4. Early peritoneal responses to MWCNT, crocidolite, and fullerene (10 days after i.p. injection):
Early findings of peritoneal cavity 10 days after i.p. administration of a) MWCNT inducing slight fibrinous deposit, adhesion, ascites retention, and edematous and hypotonic intestinal loops, b) crocidolite inducing slightly edematous intestinal loops, and c) fullerene with no obvious change except for black patchy deposits on the serosal surface.

of 6 wild-type C57BL/6 male mice each were similarly treated and sacrificed at day 10 for the observation of early peritoneal responses.

RESULTS

Although rigorously agitated prior to i.p. injection, the MWCNT sample contained aggregates among dispersed rod-shaped or fibrous particles (Fig. 2). Crocidolite sample was made of evenly dispersed rod-shaped or fibrous particles (Fig. 3a). Fullerene was in polygonal particles of micrometer size (Fig. 3b).

At day 10, the satellite groups were monitored for early responses (Fig.4). MWCNT mice showed slight fibrinous adhesion with a trace amount of ascites with scattered black spots of MWCNT aggregates. The intestine loops were edematous and hypotonic. Crocidolite mice showed similar responses but to a lesser extent, and there were no overt peritoneal adhesions. Bluish green spots of crocidolite aggregates were seen on the peritoneal surface. The Fullerene group showed minimal changes except for the black spots of aggregates on the serosal surfaces.

The vehicle control mice showed no overt change in peritoneal cavity.

The mice of main groups were monitored until one of the groups reached 100% mortality. The highest lethality

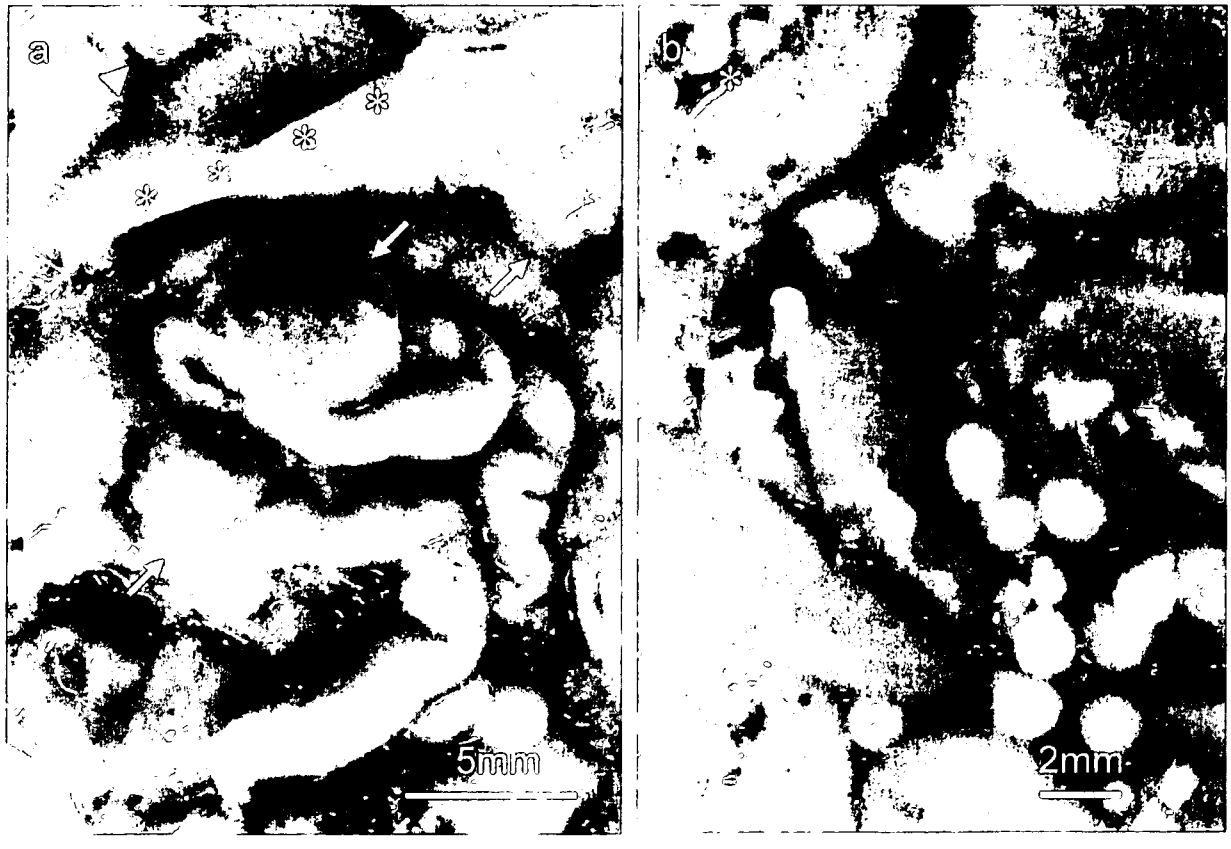

Fig. 5. Macroscopic view of abdominal viscera of MWCNT-treated and crocidolite-treated mouse:
Macroscopic view of the abdominal viscera excised *en bloc* of a) MWCNT-treated mouse that died at day 147, and b) crocidolite-treated mouse moribund on day 172 due to ileus. a) Fibrous adhesions of the visceral organs and multiple peritoneal tumor formation (arrows) are seen. Asterisks indicate the ventral cut end of diaphragma. One tumor penetrates the diaphragma and protrudes into pleural cavity (arrow head). Black spots are the aggregates of MWCNT. b) Multiple nodules up to 2 mm in diameter are induced on the serosal surface including liver (asterisk). Bluish green spots are the aggregates of crocidolite. Histology of the nodules is shown in Fig. 7a.

was seen in the MWCNT group followed by the Crocidolite group, and the study was terminated at week 25 (day 180) and all mice of the Control and the Fullerene groups and 6 of the Crocidolite group were subject to autopsy. MWCNT-treated mice revealed moderate to severe fibrous peritoneal adhesion with slight ascites, fibrous peritoneal thickening with occasional black-colored depositions and a high incidence of macroscopic peritoneal tumors up to 2.7 × 1.5 cm in size (Fig. 5a). Similar findings but to a lesser extent with bluish green deposits were seen in asbestos-treated mice. In some cases, small polyp-like nodules were seen over the serosal surface (Fig. 5b). The Fullerene group showed no peritoneal adhesion, fibrous thickening nor tumor induction. Only small black plaques were scattered on the serosal surface.

Histologically, peritoneal adhesion and fibrous thickening of the MWCNT group mice was due to the formation of fibrous scars and foreign body granulomas against the MWCNT with phagocytic cells including multinucleated giant cells. Adjacent to those fibrogranulomatous lesions, a spectrum of peritoneal mesothelial lesions was seen, from nodular mesotheliomatous pile-ups of atypical mesothelial cells (Fig. 6), typical epithelial mesotheliomas with occasional hobnail appearance and mild to moderate fibrovascular stem formation (Fig. 7a), to large tumors measuring up to 2.7 × 1.5 cm in size composed of anaplasic cells with high mitotic rate and occasional central necrosis compatible with the diagnosis of high-grade malignant mesothelioma (Fig. 7b). Large tumors are invasive to the abdominal wall, diaphragma, liver parenchyma, and pancreas, and in some cases involving the thoracic cavity. No distant metastasis was observed so far as exam-

Fig. 6. Mesothelial response in MWCNT-treated mice:
Fibrous thickening of the peritoneum and foreign body granulomas against the MWCNT with phagocytic cells including multinucleated giant cells are formed in the MWCNT-treated mouse. Mesothelial lesions were found in the vicinity of fibrosis and granulomas. Microscopic mesotheliomatous plaques on the fibrotic peritoneum above a granuloma (MWCNT-treated mouse moribund on day 144 due to multiple mesotheliomas with severe peritoneal adhesion).

ined.

Cumulative mortality rate by mesothelioma is shown in Fig. 8. Mice with large/invasive mesotheliomas considered as cause of death are plotted by Kaplan-Meier method. Second major cause of death was constriction ileus due to severe peritoneal adhesion. Among those moribund/dead or terminated at week 25, there were 3 mice with incidental mesotheliomas in the MWCNT group (cause of death: all three by ileus) and 6 incidental mesotheliomas in the Crocidolite group (cause of death: three by ileus and three terminated at week 25). The overall incidence of mesothelioma after the first incidental case found in the MWCNT group at day 84 were 14/16 (87.5%, 11 found as cause of death, 3 as incidental) in MWCNT and 14/18 (77.8%, 8 found as cause of death, 6 as incidental including 3 terminated at week 25) in the Crocidolite group. Neither tumor induction nor interim death was observed in the Control and the Fullerene groups except for one moriband mouse by chronic pyelonephritis at day 152.

In large fibrous scars/granulation, aggregates similar to those shown in Fig. 2c and 2d were found embedded. Dispersed fibers of MWCNT and crocidolite were found extracellular in the fibrotic lesions or phagocytized by the phagocytic cells. Such fiber-laden cells were found not only in the peritoneal lesions but also in the liver within the hepatic sinusoids or along with the fibrous septum between the hepatic lobes, and in the mesenteric lymph nodes (Fig. 9).

In the Fullerene group, peritoneal lesion was minimal. Only small brownish black plaques were seen on the serosal surface. Histologically, the plaques contained polygonal clefts and lacunae surrounded by a thin layer of foamy cells and separated by thin fibrous septa (Fig.10). The clefts/lacunae corresponded to the injected fullerene aggregates in size and shape. Since fullerene dissolves well in organic solvents, especially in xylene, the embedded particles were washed away during histology preparation, leaving clefts behind. It is noted that the edge of the clefts are tinted brown, indicating possible biodegradation of the surface of the fullerene particles by the phagocytic cells, blending proteins and/or other organic components so that the sub-micrometer fullerene grains become resis-

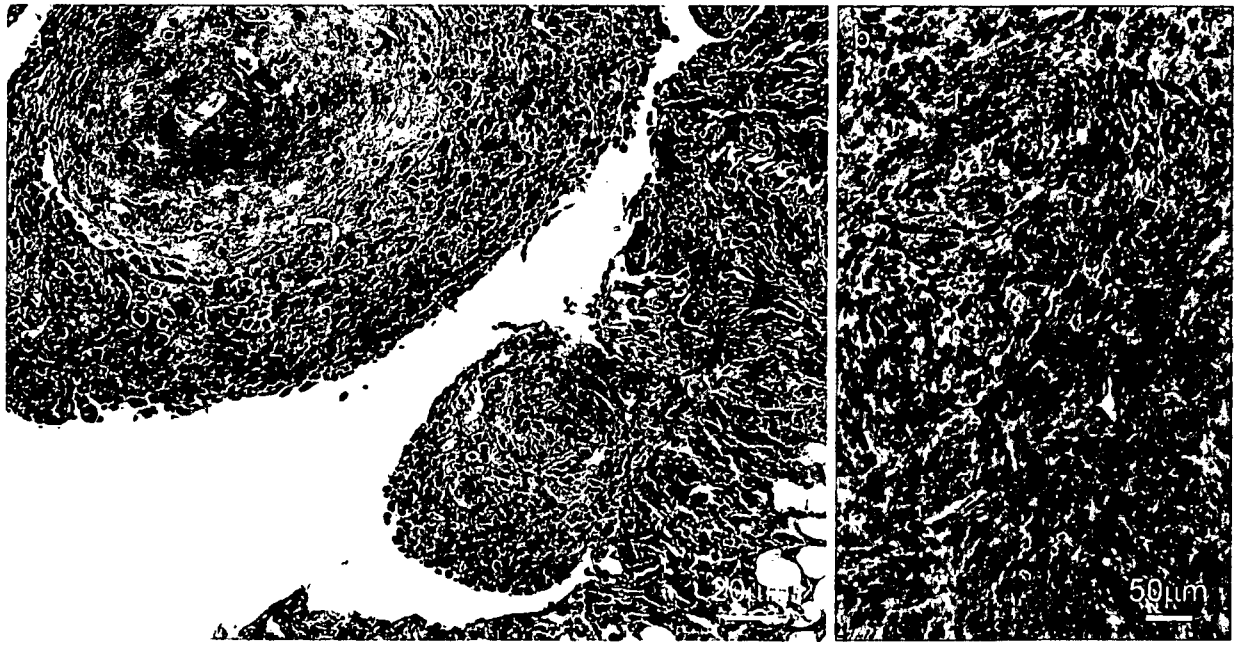

Fig. 7. Mesotheliomas in the Crocidolite group:
a) Typical mesothelioma nodules with fibrous stem induced in crocidolite-treated mouse (moribund on day 172 with multiple mesotheliomatous nodules with hemorrhagic ascites and peritoneal adhesion). b) Undifferentiated form of mesothelioma (so-called high-grade malignant mesothelioma) found as an invasive tumor of 1×1 cm in size (moribund case on day 170 with multiple invasive mesotheliomas up to 1×1.5 cm in size, severe peritoneal fibrosis and jaundice).

Mesothelioma by MWCNT in p53 +/– mouse.

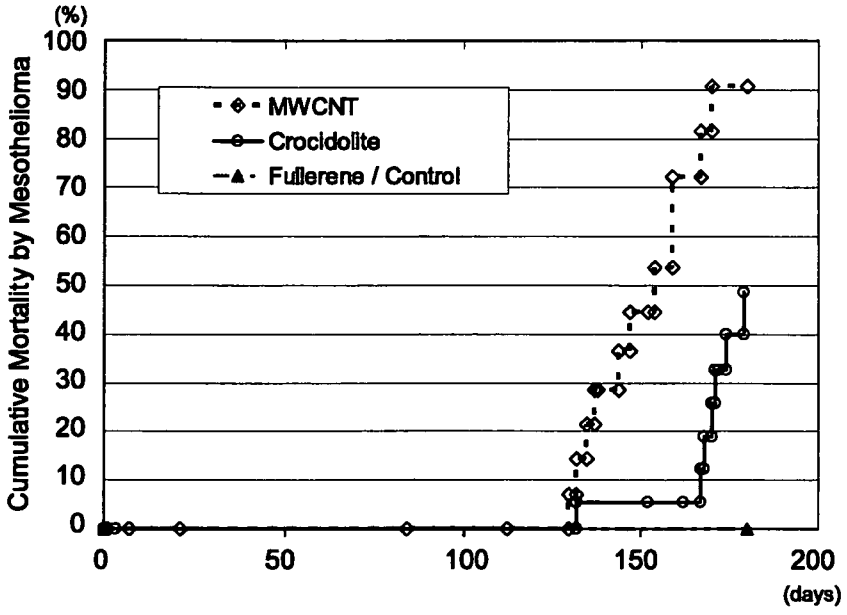

Fig. 8. Cumulative mortality of MWCNT and crocidolite treated mice by mesothelioma: Mice with large/invasive mesotheliomas considered as cause of death are plotted by Kaplan-Meier method. Second major cause of death was constriction ileus due to severe peritoneal adhesion. Among those moribund/dead or terminated at week 25 (day 180), there were 3 mice with incidental mesotheliomas in the MWCNT group and 6 incidental mesotheliomas in the Crocidolite group. No tumor induction was observed in the Fullerene and the Control groups.

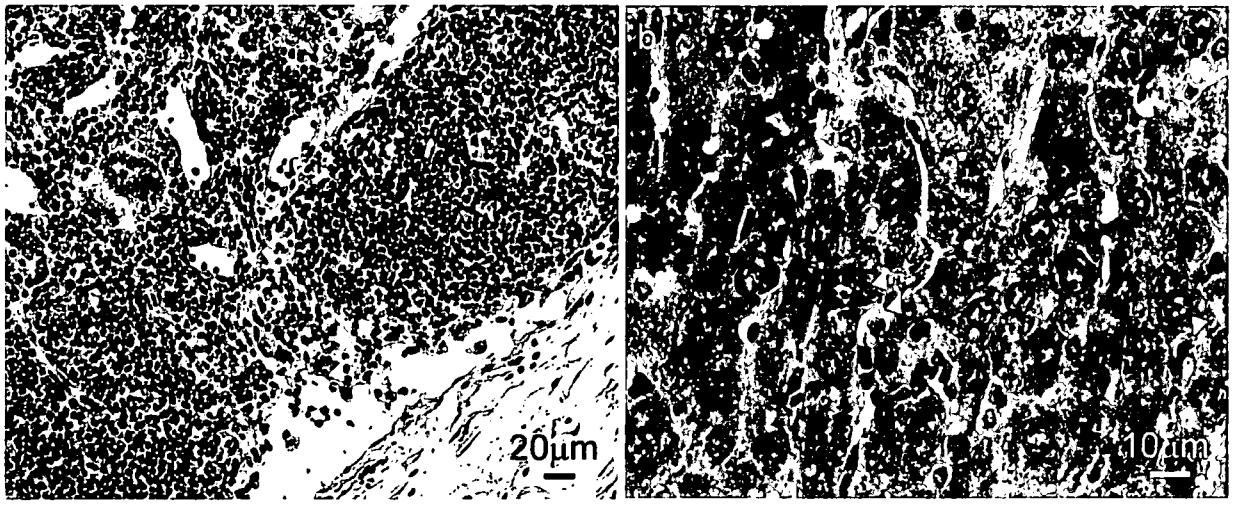

Fig. 9. Extraperitoneal migration of shorter fibers:
Phagocytized shorter fibers are found in hepatic sinusoids and local lymph nodes. a) Multinuclear giant cells (asterisks) and mononuclear phagocytic cells (arrow heads) with black fibers are seen in mesenteric lymph nodes (MWCNT-treated moribund mouse on day 159 with mesotheliomas and fibrous adhesion). b) MWCNT-laden phagocytic cells in hepatic sinusoids (arrow heads)(MWCNT-treated mouse found dead on day 84 with multiple mesotheliomas up to 0.7×0.7 cm in size, severe peritoneal fibrosis and pleural effusion).

tant to the solvents.

In summary, intraperitoneally administered MWCNT has induced mesothelioma in the p53(+/−) mice carcinogenesis model, probably due to its resemblance to asbestos in size and shape, and biopersistency.

DISCUSSION

The foreign body carcinogenesis is a category among various mechanisms of carcinogenesis. It has been postulated that ROS and/or RNS generated locally by the inflammatory reactions against non-digestive, long-lasting foreign bodies induces carcinogenic response (Tazawa *et al.*,2007). And one particular shape and size to enhance

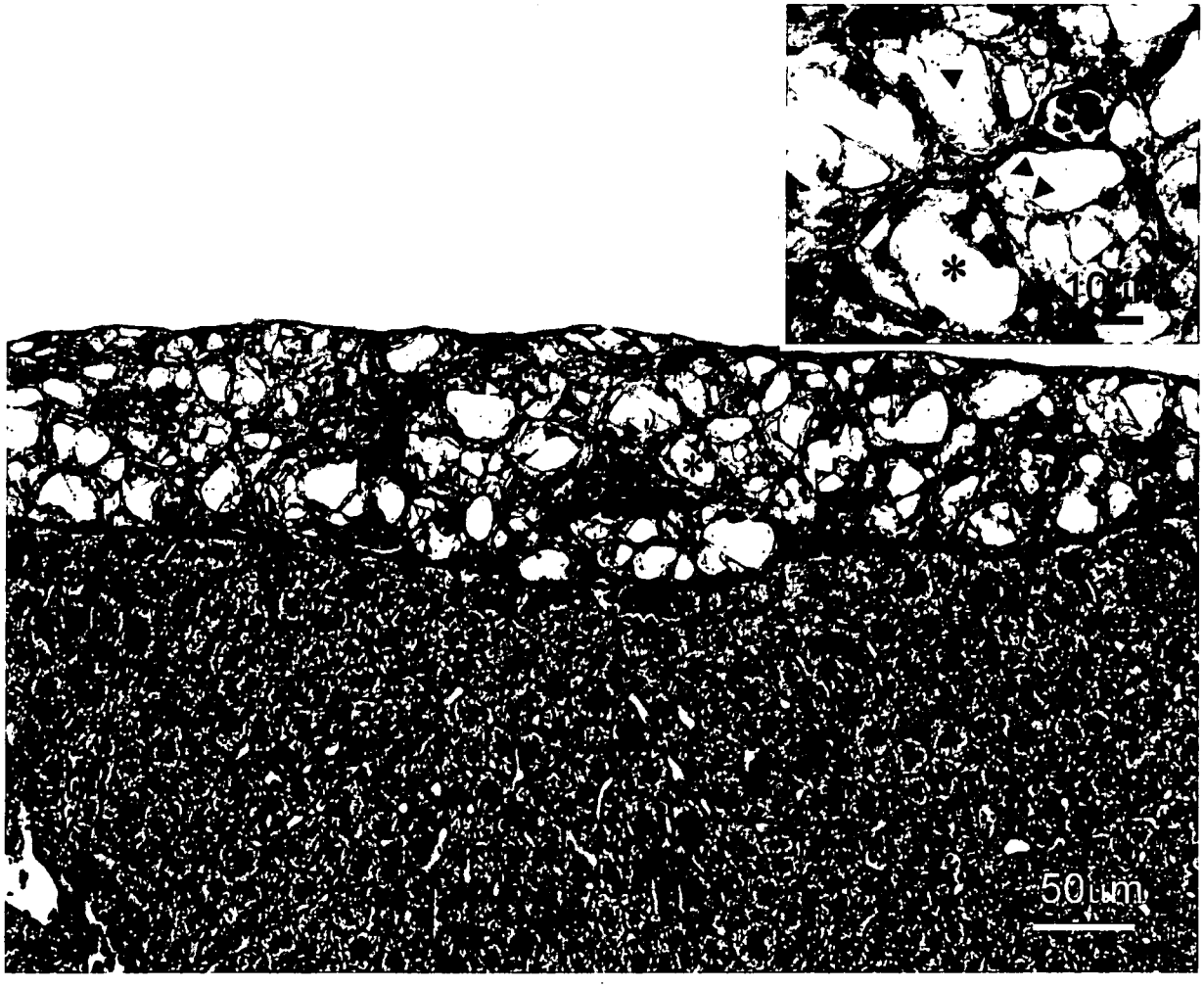

Fig. 10. Fullerene deposits:
Serosa of fullerene-treated mice showed minimum response within this 25-week period. Only black spots were occasionally seen on the surface. Histologically, the spots were made of polygonal slits surrounded by foamy cells and fibrous septa forming a compact fibrous scar. There were no signs of mesothelial response by this treatment. Since fullerene dissolves well to organic solvents especially xylene, the embedded particles were washed away leaving clefts behind. It is noted that the edges of the clefts are tinted brown, indicating possible biodegradation of the surface of the fullerene particles by the phagocytic cells, blending proteins and/or other organic components so that the sub-micrometer fullerene grains become resistant to the solvents (arrow head in inset).

this potency has been extensively studied on asbestos and man-made fibers (WHO, 1986, 1998). To study the asbestos-type carcinogenesis, the intraperitoneal route has been adopted in parallel to inhalation or transtracheal route of lung exposure. There has been some debate on whether rodent models are equivalent to the inhalation exposure to humans (Pott *et al.*,1994). Current understanding would be that the intraperitoneal model has considerable value on hazard identification in this regard (WHO, 1998, 2002). On the other hand, the p53 (+/–) mice, in general, have been suggested to be a good model to predict carcinogen, especially of a genotoxic nature (Pritchard *et al.*,2003). Relatively recently, this model has been reported to be sensitive to oxidative stress-mediated carcinogenesis such as foreign body carcinogenesis, producing a tumor with shorter latency periods than in wild-type mice (Tazawa *et al.*,2007). When asbestos was applied intraperitoneally to this model, mesotheliomas were induced with short latency as well (Marsella *et al.*,1997; Vaslet *et al.*,2002). Here, although the genotoxic effect of MWCNT is unclear, our results suggested that intraperitoneal administration of MWCNT possesses carcinogenic potential in p53(+/–) mice presumably depending on its size/shape and persistency in the organism.

Prediction of the mesotheliomagenic potential of MWCNT in humans cannot be completed by this p53+/– mouse model study. For example, glass fiber of a same shape and size to asbestos tends to fail to induce mesothelioma in humans because of its relatively faster disappearance from the deposition sites (Lippmann, 1990). Biodurability of MWCNT has to be rigorously tested before making any strong regulatory action. Likewise, Fe content of the material may be an important aspect to its carcinogenicity although our MWCNT contained lower Fe than crocidolite (WHO, 1986).

As shown in Fig.1, MWCNT studied here consists of rods and fibers of various size. In general, a bulk of a nanomaterial may contain a wide spectrum of particles at least in their size, from tens of micrometer down to true nanometer ranges. As suggested in this study by fullerene, micrometer-sized particles may become much smaller by biological activities, such as foreign body digestion activities of phagocytic cells. And yet, it is important to limit the significance of this study to the monitoring of biological activity of a compartment of the MWCNT longer than 5 micrometer. There is no information that this study method would be sensitive to pure nanometer-sized particles within this timeframe, i.e. 25 weeks. Again, this study is considered sufficient for detection of mesotheliomagenesis only by rod-shaped micrometer-sized particles. The biological effects of pure nanometer-sized CNTs and fullerene are not assessed in this study, and therefore, this remains open to further research.

The safety assessment for the new materials such as nanoparticles poses a new paradigm. The key to it is that the full-scale exposure to the public has not yet started. Therefore, there is a good chance that the information from hazard identification studies can directly be fed back to the product development plans so that harmful exposure can be prevented before it happens. In this way, manufacturers can produce safer products without risking themselves and the consumers by waiting for the full chronic toxicology studies including carcinogenicity studies to be finished after their initial (less safe) products are widely marketed.

ACKNOWLEDGMENTS

The authors thank Mr. Masaki Tsuji for technical support. This study was supported by Health Sciences Research Grants H17-kagaku-012 and H18-kagaku-ippan-007 from the Ministry of Health, Labour and Welfare, Japan.

REFERENCES

Bernstein, D.M. and Riego Sintes, J.M. (1999): Methods for the determination of the hazardous properties for human health of man made mineral fibres (MMMF). In: European Commission Joint Research Centre. Institute for Health and Consumer Protection, Unit: Toxicology and Chemical Substances. European Chemicals Bureau. pp. 44-45.

Coussens, L.M. and Werb, Z. (2002): Inflammation and cancer. Nature, **420**, 860-867.

Donaldson, K., Aitken, R., Tran, L., Stone, V., Duffin, R., Forrest, G. and Alexander, A. (2006): Carbon nanotubes: A review of their properties in relation to pulmonary toxicology and workplace safety. Toxicol. Sci., **92**, 5-22.

Gulumian, M. and van Wyk, J.A. (1987): Hydroxyl radical production in the presence of fibres by a Fenton-type reaction. Chem. Biol. Interact., **62**, 89-97.

Hei, T.K., Xu, A., Huang, S.X. and Zhao, Y. (2006): Mechanism of fiber carcinogenesis: From reactive radical species to silencing of the beta igH3 gene. Inhal. Toxicol., **18**, 985-990.

Hou, P.-X., Xu, S.-T., Ying, Z., Yang, Q.-H., Liu, C. and Cheng, H.-M. (2003): Hydrogen adsorption/desorption behavior of multi-walled carbon nanotubes with different diameters. Carbon, **41**, 2471-2476.

Jiang, L., Zhong, Y., Akatsuka, S., Liu, Y.T., Dutta, K.K., Lee, W.H., Onuki, J., Masumura, K., Nohmi, T. and Toyokuni, S. (2006): Deletion and single nucleotide substitution at G:C in the kidney of gpt delta transgenic mice after ferric nitrilotriacetate treatment. Cancer Sci., **97**, 1159-1167.

Lam, C.W., James, J.T., McCluskey, R., Arepalli, S. and Hunter, R.L. (2006): A review of carbon nanotube toxicity and assessment of potential occupational and environmental health risks. Crit. Rev. Toxicol., **36**, 189-217.

Lippmann, M. (1990): Effects of fiber characteristics on lung deposition, retention, and disease. Environ. Health Perspect., **88**, 311-317.

Luo, J., Peng, L.-M., Xue, Z.Q. and Wu, J.L. (2004): Positive electron affinity of fullerenes: Its effect and origin. J. Chem. Phys., **120**, 7998-8001.

Marsella, J.M., Liu, B.L., Vaslet, C.A. and Kane, A.B. (1997): Susceptibility of p53-deficient mice to induction of mesothelioma by crocidolite asbestos fibers. Environ. Health Perspect., **105** (Suppl. 5), 1069-1072.

Moalli, P.A., MacDonald, J.L., Goodglick, L.A. and Kane, A.B. (1987): Acute injury and regeneration of the mesothelium in response to asbestos fibers. Am. J. Pathol., **128**, 426-445.

Pott, F., Roller, M., Kamino, K. and Bellmann, B. (1994): Significance of durability of mineral fibers for their toxicity and carcinogenic potency in the abdominal cavity of rats in comparison with the low sensitivity of inhalation studies. Environ. Health Perspect., **102** (Suppl. 5), 145-150.

Pritchard, J.B., French, J.E., Davis, B.J. and Haseman, J.K. (2003): The role of transgenic mouse models in carcinogen identification. Environ. Health Perspect., **111**, 444-454.

Roller, M., Pott, F., Kamino, K., Althoff, G.H. and Bellmann, B. (1997): Dose-response relationship of fibrous dusts in intraperitoneal studies. Environ. Health Perspect., **105** (Suppl. 5), 1253-1256.

Tazawa, H., Tatemichi, M., Sawa, T., Gilibert, I., Ma, N., Hiraku, Y., Donehower, L.A., Ohgaki, H., Kawanishi, S. and Ohshima, H. (2007): Oxidative and nitrative stress caused by subcutaneous implantation of a foreign body accelerates sarcoma development in Trp53+/– mice. Carcinogenesis, **28**, 191-198.

Tsukada, T., Tomooka, Y., Takai, S., Ueda, Y., Nishikawa, S-I., Yagi, T., Tokunaga, T., Takeda, N., Suda, Y., Abe, S., Matsuo, I., Ikawa, Y. and Aizawa, S-I. (1993): Enhanced proliferative potential in culture of cells from p53-deficeint mice. Oncogene, **8**, 3313-3322.

Vaslet, C.A., Messier, N.J. and Kane, A.B. (2002): Accelerated progression of asbestos-induced mesotheliomas in heterozygous p53+/– mice. Toxicol. Sci., **68**, 331-338.

World Health Organization (1986): Environmental Health Criteria, **53**. Asbestos and Other Natural Mineral Fibres. World Health Organization, Geneva.

World Health Organization (1998): Environmental Health Criteria, **203**. Chrysotile Asbestos. World Health Organization, Geneva.

World Health Organization (2002): Man-made vitreous fibres. IARC monographs on the evaluation of carcinogenic risk to humans, Vol., **81**, IARC Lyon.

nature
cell biology

MesP1 drives vertebrate cardiovascular differentiation through Dkk-1-mediated blockade of Wnt-signalling

R. David[1], C. Brenner[1,7], J. Stieber[2], F. Schwarz[1], S. Brunner[1], M. Vollmer[3], E. Mentele[4], J. Müller-Höcker[5], S. Kitajima[6], H. Lickert[3], R. Rupp[4] and W.-M. Franz[1]

ES-cell-based cardiovascular repair requires an in-depth understanding of the molecular mechanisms underlying the differentiation of cardiovascular ES cells. A candidate cardiovascular-fate inducer is the bHLH transcription factor MesP1[1,2]. As one of the earliest markers, it is expressed specifically in almost all cardiovascular precursors and is required for cardiac morphogenesis[2,3]. Here we show that MesP1 is a key factor sufficient to induce the formation of ectopic heart tissue in vertebrates and increase cardiovasculogenesis by ES cells. Electrophysiological analysis showed all subtypes of cardiac ES-cell differentiation[4]. MesP1 overexpression and knockdown experiments revealed a prominent function of MesP1 in a gene regulatory cascade, causing Dkk-1-mediated blockade of canonical Wnt-signalling. Independent evidence from ChIP and *in vitro* DNA-binding studies, expression analysis in wild-type and *MesP* knockout mice, and reporter assays confirm that *Dkk-1* is a direct target of MesP1. Further analysis of the regulatory networks involving MesP1 will be required to preprogramme ES cells towards a cardiovascular fate for cell therapy and cardiovascular tissue engineering. This may also provide a tool to elicit cardiac transdifferentiation in native human adult stem cells.

Current therapeutic modalities for degenerative cardiovascular diseases are limited. They include medical therapy, mechanical left-ventricular assist devices and cardiac transplantation. Embryonic stem (ES) cells, which can differentiate into functional cardiovascular cells, may enable transplantation of cardiovascular cells [5]. The proliferative potential of cardiomyocytes derived from ES cells is limited, and reasonable yields to repair an infarction in humans (>10^8 cardiomyocytes) are yet to be achieved[6].

It is crucial, therefore, to understand the biological processes leading to formation of cardiovascular cells. A candidate key cardiovascular-fate inducer is the basic helix-loop-helix (bHLH) transcription factor, MesP1, which is expressed in almost all precursors of the cardiovascular system. It is required for cardiac morphogenesis and is currently the earliest marker of the cardiovascular lineage[1,2,7]. MesP1-deficient mice show aberrant heart morphogenesis that resulted in cardia bifida[1] and misexpression of Flk1 (VEGFR-2 or KDR), one of the receptors for VEGF[1]. In the primitive chordate *Ciona savignyi*, the sole known orthologue of vertebrate *MesP* genes in ascidians (*Cs-MesP*) is essential for specification of heart precursor cells expressing *Nkx*, *HAND* and *HAND*-like genes. Morpholino-based knockdown of *Cs-MesP* causes failure of the development of the juvenile heart[8]. A constitutively active Cs-MesP induced cardiogenesis independently of cardiac precursor-cell migration in *Ciona*[9]. This suggests a mechanism for cardiovascular specification that is highly conserved in chordates and initiated by *MesP* genes, with factors such as Nkx, HAND and Flk1 acting further downstream.

We therefore hypothesized that cardiovasculogenesis in vertebrates not only requires correct MesP1 expression, but also that this factor might be a master regulator sufficient to induce cardiovasculogenesis. Here, we show from different experimental systems using vertebrate embryos, as well as ES cells and *in vitro* studies, that this is indeed the case.

We first injected MesP1 overexpression-plasmid DNA into one blastomere of two-cell *Xenopus laevis* embryos. This caused the formation of ectopic beating tissue in various regions of developed tadpoles (Supplementary Information, Movies 1–4). The beating rhythm of the specimen (Supplementary Information, Movie 1) indicated that the contracting tissue in the head region was electrically coupled to the heart, whereas ectopic beating (Supplementary Information, movies Movies 2, 3) showed autonomous rhythms. Whole-mount *in situ* hybridization for myosin light chain (MLC) mRNA confirmed ectopic formation of cardiomyocytes in tadpoles that overexpressed MesP1 (Fig. 1b–e), compared with control tadpoles (Fig. 1a).

Relying on the high conservation of vertebrate MesP1 proteins, we used human MesP1 in mouse ES cells as it would be easily traced. We inserted human *MesP1* cDNA in pIRES-EGFP-2 for overexpression in ES cells (Fig. 2a), simultaneously allowing detection of ES-cell clones using

[1]Medizinische Klinik und Poliklinik I, Klinikum Großhadern der LMU, D-81377 München, Germany. [2]Lehrstuhl für Pharmakologie und Toxikologie der Universität Erlangen, D-91054 Erlangen, Germany; [3]GSF - National Research Center for Environment and Health, D-85764 Neuherberg, Germany. [4]Adolph-Butenandt-Institut der LMU, D-80336 München, Germany. [5]Pathologisches Institut der LMU, D-80337 München, Germany. [6]Division of Cellular & Molecular Toxicology, Biological Safety Research Center, National Institute of Health Sciences 1-18-1 Kamiyohga, Setagaya-ku, Tokyo 158-8501, Japan.
Correspondence should be addressed to R.D. or W.-M.F. (e-mail: robert.david@med.uni-muenchen.de; wolfgang.franz@med.uni-muenchen.de)

Received 6 December 2007; accepted 28 January 2008; published online 24 February 2008; DOI: 10.1038/ncb1696

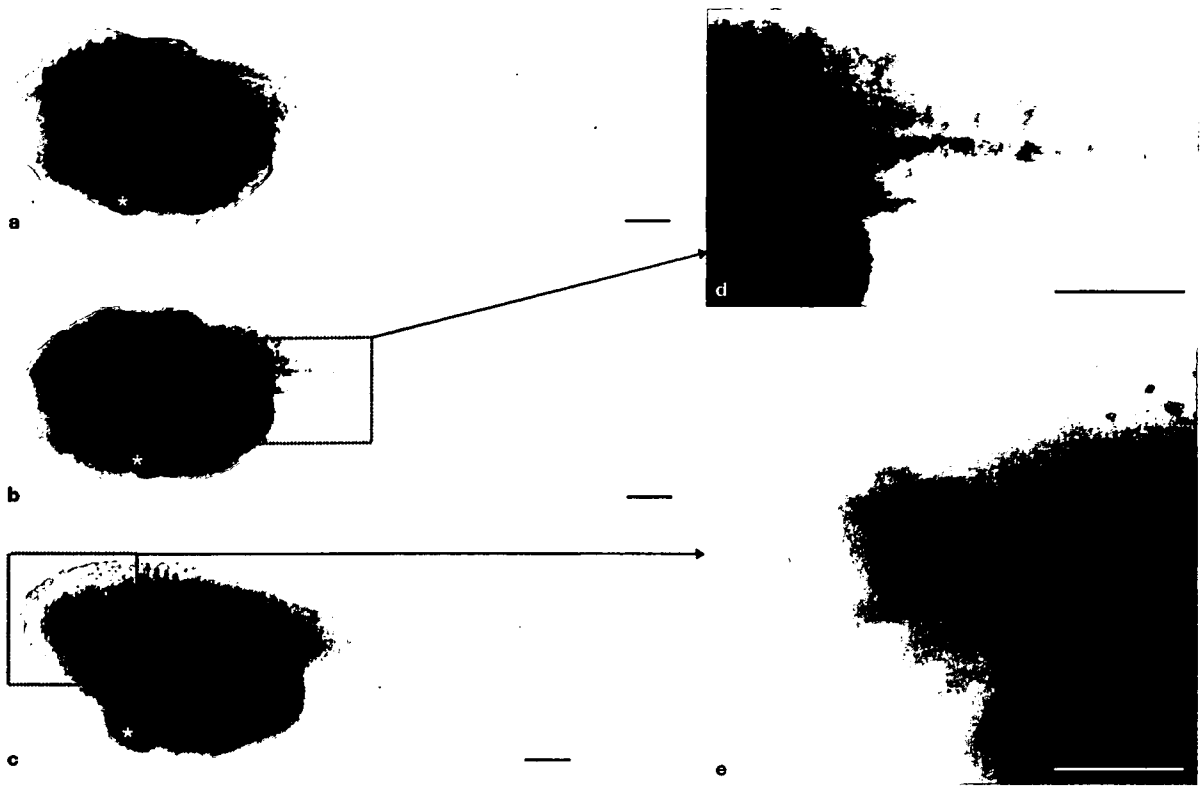

Figure 1 MesP1 overexpression in *Xenopus* induces ectopic cardiac tissue. (**a**) MLC *in situ* hybridization using a stage 45 *Xenopus* control tadpole previously injected with 100 pg EGFP expression plasmid into one blastomere at two-cell stage. * Specific staining of *MLC* mRNA within the heart. (**b**, **c**) MLC *in situ* hybridization using stage 45 *Xenopus* tadpoles injected with 100 pg MesP1 overexpression plasmid. Specific staining of *MLC* mRNA in the heart (*) was paralleled by MLC expression in the trunk region (**b**, boxed area) and in the dorsal part of a partially ablated eye on the injected side (**c**, boxed area). (**d**) Higher magnification of ectopic MLC expression in specimen **b**. (**e**) Higher magnification of MLC expression in the eye region shown for specimen **c**. Scale bars are 0.5 mm.

EGFP (enhanced green fluorescent protein; Fig. 2b, c). Overexpression of MesP1 was confirmed at the mRNA (Fig. 2d) and protein levels (Fig. 2e). RT-PCRs showed no influence on *Oct4*, *Nanog* and *Rex-1* mRNA levels, compared with control transfected cells, which were normal, undifferentiated colonies grown in medium containing leukaemia inhibitory factor (LIF; Fig. 2f). These results suggest that MesP1 alone is not sufficient to induce germ-layer-specific differentiation.

We then verified the time course of cytomegalovirus (CMV) promoter activity used in our overexpression construct: fluorescence activated cell sorting (FACS) analyses for EGFP expression showed that 89% of the cells were EGFP-positive at day 0 of differentiation and 12% were positive at day 4 (Supplementary Information, Fig. S1). This is consistent with the known silencing of the CMV promoter in differentiating ES cells.

During differentiation, clones that overexpressed MesP1 began to contract earlier and showed approximately five-fold more contracting areas, compared with the controls (Fig. 3a, Supplementary Information, Movies 5, 6). This exceeds the *in vitro* yield reported in previous studies, in which, ES-cell-derived cardiomyocytes were increased two- to three-fold by treatment with retinoic acid[10], nitric oxide or an inducible nictic oxide synthase[11]. Similarly, in a study where cells had to be preselected for Flk1 using FACS[12], increased cardiomyogenesis was observed in ES cells lacking RBP-J, a key downstream element in the Notch signalling pathway.

Cardiomyocytes that overexpressed MesP1 showed normal patterns of the cardiac sarcomeric marker αMHC (Fig. 3b–d). Ultrastructure of the cells with typical myocytic features revealed parallel arrays of myofibrillar bundles inserting into Z-disc-like bands (Fig. 3e). Similarly, intercellular contacts, probably corresponding to gap junctions, were detected (Fig. 3f).

In addition to increased beating, the MesP1-transfected ES-cell clones showed highly increased spontaneous sprouting of structures from embryoid bodies (EBs), which resembled vascular cells (Fig. 3g–j), a feature normally induced in sprouting assays by addition of VEGF, FGF2 and erythropoietin in collagen I gel matrices[13]. These cells migrated out of the EBs and showed typical expression of von Willebrand factor (vWF; Fig. 3h, i). Our observation is consistent with the knowledge that cardiac and vascular cells share the same embryonic origin in the lateral plate mesoderm and that mouse MesP1 has been described as a marker for both cardiac- and endothelial-cell precursors[1].

We next investigated whether our observations are consistent with mRNA expression patterns and found enhanced expression of transcripts encoding the early cardiac transcription factors Nkx 2.5, GATA 4 and Mef2c (Fig. 4a). mRNAs encoding the cardiac structural proteins and hormones connexin 45, connexin 43, MLC2v, TnI, ANF and TTR, were markedly increased (Fig. 4a). Additionally, at day 6, mRNA levels

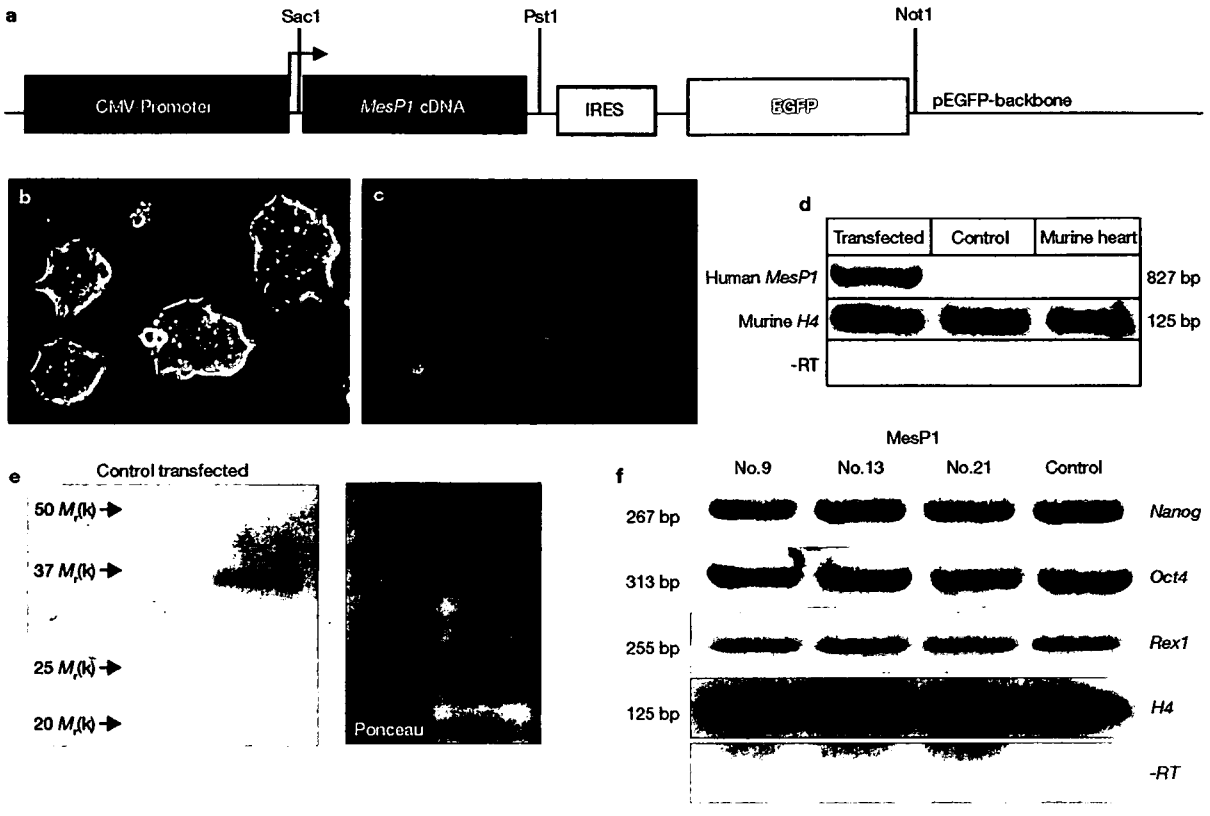

Figure 2 Functionality of the MesP1 overexpression construct in ES cells. (**a**) Transfection construct bearing the human *MesP1–IRES–EGFP* cassette. (**b**, **c**) Stably transfected mouse ES cell colonies showing EGFP fluorescence. (**d**) RT-PCR for overexpressed human *MesP1* mRNA in stably transfected mouse ES cells. (**e**) Verification of hMesP1 overexpression in mouse ES cells on the protein level. Full scans shown in Supplementary Information, Fig. S6. (**f**) RT-PCR using cDNA from undifferentiated ES cell clones: relative expression levels of pluripotency markers in the presence of LIF show no difference compared with EGFP control transfected cells. Full scans shown in Supplementary Information, Fig. S6.

for VE-cadherin were increased (Fig. 4a), correlating with the increased vascular sprouting described above (Fig. 3g–j). Downregulation of the skeletal muscle marker MyoD was also observed, indicating a shift towards the lateral plate mesoderm (Fig. 4a). An increase in the number of cells expressing the proteins α-actinin, cardiac MLC-1, TnI and CD31 (PECAM) confirmed our mRNA data (Fig 4b–d; Supplementary Information, Fig. S4C).

In the non-mesodermal lineages, neural differentiation seemed to be increased in MesP1-overexpressing cells, as shown for *NeuroD* and *Neurogenin* mRNAs. Correspondingly, epidermis formation in ectodermal ES-cell descendents seemed to be diminished, as indicated by the decreased expression of cytokeratin17 (Fig. 4a). This observation is consistent with the known neural-inducing potential of cardiogenic cells[14]. Expression of hepatocyte nuclear factor 4 (HNF4) was not altered, suggesting that endodermal differentiation was unaffected (Fig. 4a).

Electrophysiological analysis of isolated beating cardiomyocytes revealed that the three main cell types described for the near-terminally differentiated state of EB cardiomyocyte development (namely, ventricle-like, atrial-like and sinoatrial/atrioventricular (pacemaker-like) cells, as well as intermediate cells) are present in preparations from MesP1-overexpressing ES-cell clones (Supplementary Information, Fig. S2, Table S1). The action potentials generated by the respective cell types of MesP1 and control cells did not differ significantly with respect to their distinct parameters, such as maximum diastolic potential, diastolic depolarization rate, upstroke velocity or action potential plateau duration, or in their reaction to β-adrenoceptor (isoprenaline) and muscarinic-receptor (carbachol) stimulation. This supports the notion of correct cardiomyocyte development. In knockdown experiments using human *MesP1*-specific short hairpin (sh) RNA, the appearance of beating foci in shRNA-expressing ('rescued') ES cells, was reversed to control levels (Supplementary Information, Fig. S4A, B), corresponding to a reduction of TnI-expressing cells to a level similar to control numbers (Supplementary Information, Fig. S4C).

To identify direct targets of MesP1, we next performed a ChIP screen with subsequent cloning and sequencing of the unknown precipitated DNA fragments[15]. We identified two regions derived from the mouse Dkk-1 upstream region containing classical bHLH-binding motifs, which are highly conserved in humans, chickens and zebrafish *Dkk-1* genes (Supplementary Information, Fig. S5A). We then verified their specific enrichment in the precipitated DNA using PCR (Fig. 5a) and performed electrophoretic mobility shift assays (EMSAs) to confirm specific MesP1-binding to these elements *in vitro* (Fig. 5b). To investigate the relevance of these observations *in vivo*, we performed whole-mount *in situ* hybridization using embryonic day (E) 7.5 mouse

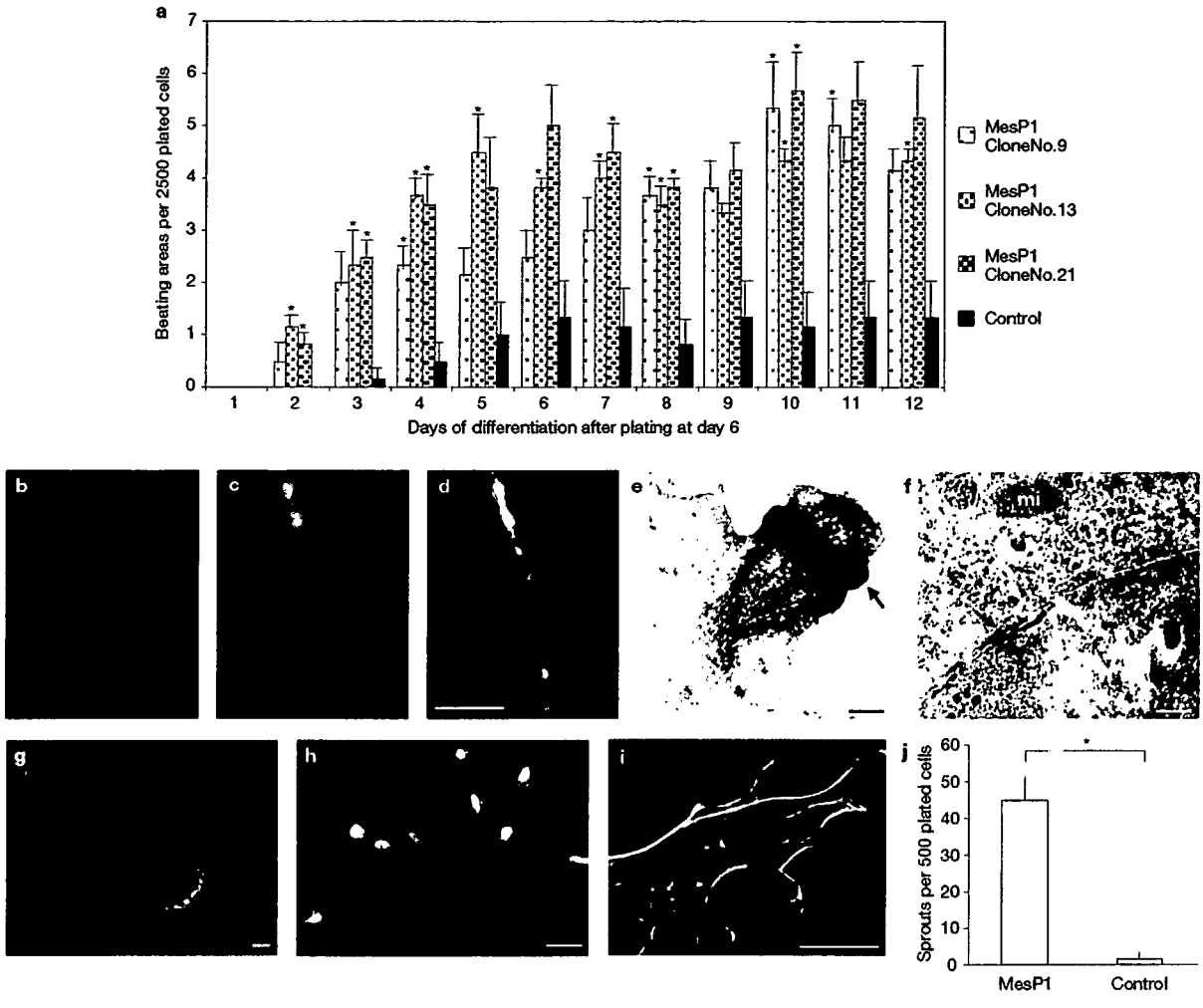

Figure 3 Increased appearance of cardiomyocytes and endothelial cells in MesP1-overexpressing ES cells. (**a**) Increase of spontaneous beating activity in three independent mouse ES cell clones stably transfected with the *MesP1–IRES–EGFP* construct. (**b**) Confocal analysis of αMHC expression in a cardiomyocyte overexpressing MesP1. (**c**) Counterstaining against actin. (**d**) Overlay of αMHC and actin staining. Scale bar is 5 μm. (**e**) Electron microscopy: straight fibrils composed predominantly of thick filaments (myosin) and formation of a Z-line (→) in the subplasmalemmal zone. Scale bar is 0.5 μm. (**f**) Intercellular junctions between two cells with subplasmalemmal densities (→) and longitudinal aggregates of thin filaments (*). The gap was narrowed at the contact sites, consistent with an attenuated gap junction. mi = Mitochondrium. Scale bar is 0.5 μm. (**g**) Spontaneous sprouting of vascular-like cells from an EB at day 10 of differentiation without any addition of angiogenic growth factors. Scale bar is 30 μm. (**h**) Staining of spontaneously sprouting vascular-like cells for vWF. Nuclei were counterstained with DAPI. Scale bar is 30 μm. (**i**) Overlay of confocal microscopic analysis of vWF expression (red) and actin expression (green) in spontaneously sprouting vascular like cells. Scale bar is 10 μm. (**j**) Quantification of spontaneous sprouting at day 10 of differentiation in MesP1-overexpressing and EGFP-overexpressing ES-cell clones (data are mean ± s. d., $n = 3$, $P = 0{,}0029$).

embryos, in which we found co-expression of MesP1 and Dkk-1 in the cardio-cranial mesoderm precursors[1] migrating laterally from the primitive streak towards the anterior region (Fig. 5c). Additionally, *MesP1* mRNA was found at the base of the allantois. At the same developmental stage, Dkk-1 was expressed in the anterior visceral endoderm, the anterior cardio-cranial mesoderm and at the base of the allantois (Fig. 5c, upper panels). Histological sections from these specimens show *MesP1* mRNA in posterior and lateral mesoderm populations giving rise to cardio-cranial mesoderm. Similarly, Dkk-1 was expressed in lateral and anterior cardio-cranial mesoderm populations (Fig. 5c, lower panels), demonstrating an overlapping expression domain with MesP-1 in this region.

We then analysed mRNA expression patterns at an earlier stage of ES-cell differentiation (day 3). Again, we found upregulation of *Nkx2.5* and *GATA4* mRNAs in ES cells overexpressing MesP1. In contrast to unaltered *brachyury* mRNA levels at day 3, the amounts of *Dkk-1* and *Hex* mRNAs were markedly increased (Fig. 5d).

To determine whether MesP1 can initiate cardiomyogenesis even in the absence of general mesoderm-inducing factors, we performed FACS analyses for Flk1, the earliest surface marker for the lateral mesoderm[16], during ES-cell differentiation. Few (0.2–0.25%) cells were found to express Flk1 in undifferentiated MesP1 and control clones. The Flk1-positive population did not increase significantly until day 4 of differentiation, when lateral and paraxial mesoderm have formed[17]. However,